Bulletin of Volcanology (2023) 85:64
https://doi.org/10.1007/s00445-023-01666-9

RESEARCH ARTICLE

Surface fractures generated during the 2021 Reykjanes oblique rifting event (SW Iceland)

Simon Bufféral[1,2] · Elisabetta Panza[1] · Stefano Mannini[1] · Ásta Rut Hjartardóttir[3] · Adriano Nobile[4] · Nils Gies[5,6] · Birgir Vilhelm Óskarsson[5] · Joël Ruch[1]

Received: 4 December 2022 / Accepted: 9 August 2023 / Published online: 21 October 2023

Abstract

We use a comprehensive dataset of field observations, high spatial resolution drone orthomosaics and digital terrain models (DTMs) to map, quantify and characterize the extensive ground fracturing related to the 2021 seismo-tectonic and volcanic activity in the Reykjanes Peninsula (Iceland). The dataset, spans an area of about 30 km^2, where we map nearly 20 000 ground cracks with metric to decametric lengths and centimetric extensional offsets, revealing a dominant dextral shear, in agreement with published seismic data. Although striking in a direction similar to the volcanic systems in the Reykjanes Peninsula (N030–040), most fractures appear as en-échelon structures globally aligned along N-S-striking fault zones up to 3–4 km long. By examining the timing of ground fracturing through repeated field observations, seismic data and InSAR images, we associate a fracture zone with most earthquakes of $M_\omega \geq 5.0$ that occurred in the month preceding the March 2021 Fagradalsfjall eruption. We describe three preexisting N-S fault zones, with fault segments that were reactivated up to three times during the pre-eruptive seismic activity, while the magma intrusion did not trigger graben-related ground fractures typically observed during magmatic injections. Our depiction of a system dominated by strike-slip tectonic features helps in understanding the geometry and bookshelf-mode of tectonic activity along a diffuse and highly oblique extensional plate boundary. Evidence of transient fracturing is typically quickly lost because of erosion or lava flow burial, highlighting a potential under-representation of diffuse fracturing when studying old tectonic and volcanic systems.

Résumé

Dans cette étude, nous combinons des observations de terrain, des images de drone de haute résolution et des modéles numériques de terrain pour cartographier et caractériser les fractures de surface provoquées par la crise sismo-tectonique et volcanique survenue en 2021 sur la péninsule de Reykjanes (Islande). Sur une zone d'environ 30 km^2, nous identifions prés de 20 000 fractures de longueur métrique à décamétrique et d'ouverture centimétrique, traduisant en grande majorité un cisaillement dextre, en accord avec les séismes majeurs ayant précédé l'éruption de Fagradalsfjall en mars 2021. Bien qu'orientées de maniére similaire aux systémes volcaniques de Reykjanes (N030-040), la plupart de ces fractures s'alignent en échelon le long de zones de faille orientées N-S et mesurant jusqu'à 3 à 4 km de longueur. En examinant la chronologie de leur mise en place grâce à nos observations répétées, aux données sismiques et à nos images InSAR, nous avons pu associer chaque zone de fracturation à des séismes de magnitude $M_\omega \geq 5.0$ survenus lors de la crise. Nous décrivons trois principales

Editorial responsibility: A. Cannata

This paper constitutes part of a topical collection: Low intensity basalt eruptions: the 2021 Geldingadalir and 2022 Meradalir eruptions of the Fagradalsfjall Fires, SW Iceland.

✉ Simon Bufféral
simon.bufferal@ens.fr

Extended author information available on the last page of the article

zones de faille N-S préexistantes, dont certains segments ont été réactivés jusqu'à trois fois durant l'activité pré-éruptive, sans pour autant générer de structures extensives classiques telles que l'ouverture d'un graben. Ainsi, notre cartographie et notre description de ce dense réseau de structures principalement décrochantes illustrent la géométrie et l'activité tectonique d'une limite de plaque extensive diffuse et fortement oblique. Grâce à notre intervention rapide sur site, nous mettons en évidence l'importance de ces fractures transitoires d'ordinaire rapidement effacées par l'érosion ou enfouies sous des coulées de lave, soulignant une sous-représentation potentielle de ce type de défomation diffuse lors de l'étude de systémes sismiques et/ou volcaniques obliques anciens.

Keywords Ground fracture · Surface faulting · Fault geometry · Slip deficit · Volcanic fissure · Volcano-tectonics · Seismicity

Introduction

Mid-oceanic ridges were first described by Marie Tharp in 1959 (Heezen et al. 1959) and later played a crucial role in developing the theory of plate tectonics (Le Pichon 1968; Tharp et al. 1968). Their typical location at ocean depths of more than 2.5 km, however, limits our ability to apply morphological or structural studies and hampers geodetic approaches, leaving many structural aspects poorly constrained, especially in cases of rift obliquity or overlapping segments. 80% of ridges have an oblique rifting direction, i.e., 10° to 80° with respect to the direction of plate divergence (Philippon and Corti 2016). Additionally, extensional plate boundaries are segmented (MacDonald et al. 1988), with rift segments separated by relay zones with offsets ranging from a few kilometers to thousands of kilometers (La Rosa et al. 2019). These relay zones are often associated with transform faults, i.e., lithospheric-scale strike-slip faults parallel to the direction of plate divergence (Wilson 1965). When two rift segments overlap or are separated by less than a few tens of kilometers, non-transform relay zones tend to accommodate the linkage between opening zones, resulting in complex rotational tectonics that combine extension and shear (Withjack and Jamison 1986; Tron and Brun 1991; Zwaan and Schreurs 2020).

Several models have been proposed to explain deformation at rift systems. One involves sets of *bookshelf-mode* strike-slip faults striking sub-parallel to the rift direction and almost orthogonal to the extension direction, which accommodate the shear component of extension, (Einarsson 2008; Green et al. 2014). Examples can be seen in the South Icelandic Seismic Zone (SISZ in Fig. 1) and in the northern part of Iceland. Pagli et al. (2019) have also proposed that the connection between the Red Sea and the Gulf of Aden involves strike-slip tectonics perpendicular to rift termination, resulting in a series of en-échelon pull-apart basins parallel to the rift. Finally, La Rosa et al. (2019) have described two rift segments connected by a shear zone characterized by two sets of conjugate oblique strike-slip faults.

Fully understanding these systems requires a geodetic and morpho-structural approach, which is challenging given their location at the ocean floor. However, progress can be made by examining the only available emerged ridges, in the Afar region and Iceland, which result from the interaction between a ridge and a hotspot (Wright et al. 2012; Poore et al. 2011; Furman et al. 2006; Bourgeois et al. 2005).

In Iceland, the Mid-Atlantic Ridge is characterized by a series of volcanic systems producing an average of one rift eruption every 3 to 5 years, and related to continuous background seismic activity (Thordarson and Larsen 2007; Jakobsdóttir 2008; Sigmundsson et al. 2020). The ridge extends west of Iceland, but it aligns with the Icelandic Hotspot (IH in Fig. 1) beneath the Vatnajökull glacier. This association triggers a displacement of the plate boundary toward the east (Einarsson 1991; Wolfe et al. 1997). Consequently, the Reykjanes Ridge (RR in Fig. 1), initially oriented N030 offshore of the Reykjanes Peninsula, undergoes a strong reorientation upon reaching the coast, aligning along a N070 axis (Clifton and Kattenhorn 2006). In this region, the North-America/Eurasia plate divergence follows a N100-N105 direction (DeMets et al. 2010; Sigmundsson et al. 2020). As a result, the plate boundary is not perpendicular to the divergence direction, but intersects it at an angle of approximately 30°—a significant deviation from the typical 90° angle.

This configuration results in the plate boundary displaying characteristics akin to a left-lateral strike-slip shear zone (Fig. 1), marked by a series of about six oblique and structurally overlapping magmatic systems (Clifton and Kattenhorn 2006). These magmatic systems are oriented approximately N035 (see Fig. 1), i.e., with a ∼25° obliquity with respect to the theoretical ideal rift direction. The main systems are, from west to east: Reykjanes; Svartsengi (-Grindavík); Fagradalsfjall; Krýsuvík-Trölladyngja (-Kleifarvatn); Brennisteinsfjöll or Bláfjöll, and Hengill (Jakobsson et al. 1978; Einarsson and Sæmundsson 1987; Sæmundsson et al. 2020). Since these systems are oblique and largely overlapping, they provide valuable information about the termination and linkage between rift segments. The Reykjanes Peninsula rift zones also comprise right-lateral strike-slip fault systems, oriented approximately N010, with a *bookshelf mode* character. This dextral system may have

a magmatic expression (Einarsson 2008) and is evident in micro-seismic data (Keiding et al. 2009; Björnsson et al. 2020).

Between December 2019 and June 2021, the North-America/Eurasia plate boundary experienced tectonic unrest at the Reykjanes Peninsula (Fig. 1), causing seismic and volcanic activity at the Svartsengi and Fagradalsfjall systems, which peaked between February 24, 2021, and March 16, 2021 (Fischer et al. 2022; Sigmundsson et al. 2022). Both the seismic and volcanic activity were accompanied by elastic and anelastic deformation, resulting in diffuse deformation and widespread ground fracturing, respectively. This activity provided us with an opportunity to better understand the relationship between tectonic processes and volcanic eruptions. We here present and analyze ground fracture data, focusing on three areas that were characterized by the highest tectonic activity (Fig. 2):

- The Beinavörðuhraun plain (hereafter West Zone, WZ), which is located 3 km west of the eruptive fissures, and below which two major pre-eruptive earthquakes occurred;
- The Mount Fagradalsfjall (FM), which is located immediately west of the eruptive fissures, and where pre-existing faults were reactivated;
- The Leggjarbrjótshraun plain (hereafter East Zone, EZ), situated 1.5 km east of the volcano and ~2 km southwest of the preliminary epicenter of the main earthquake of the

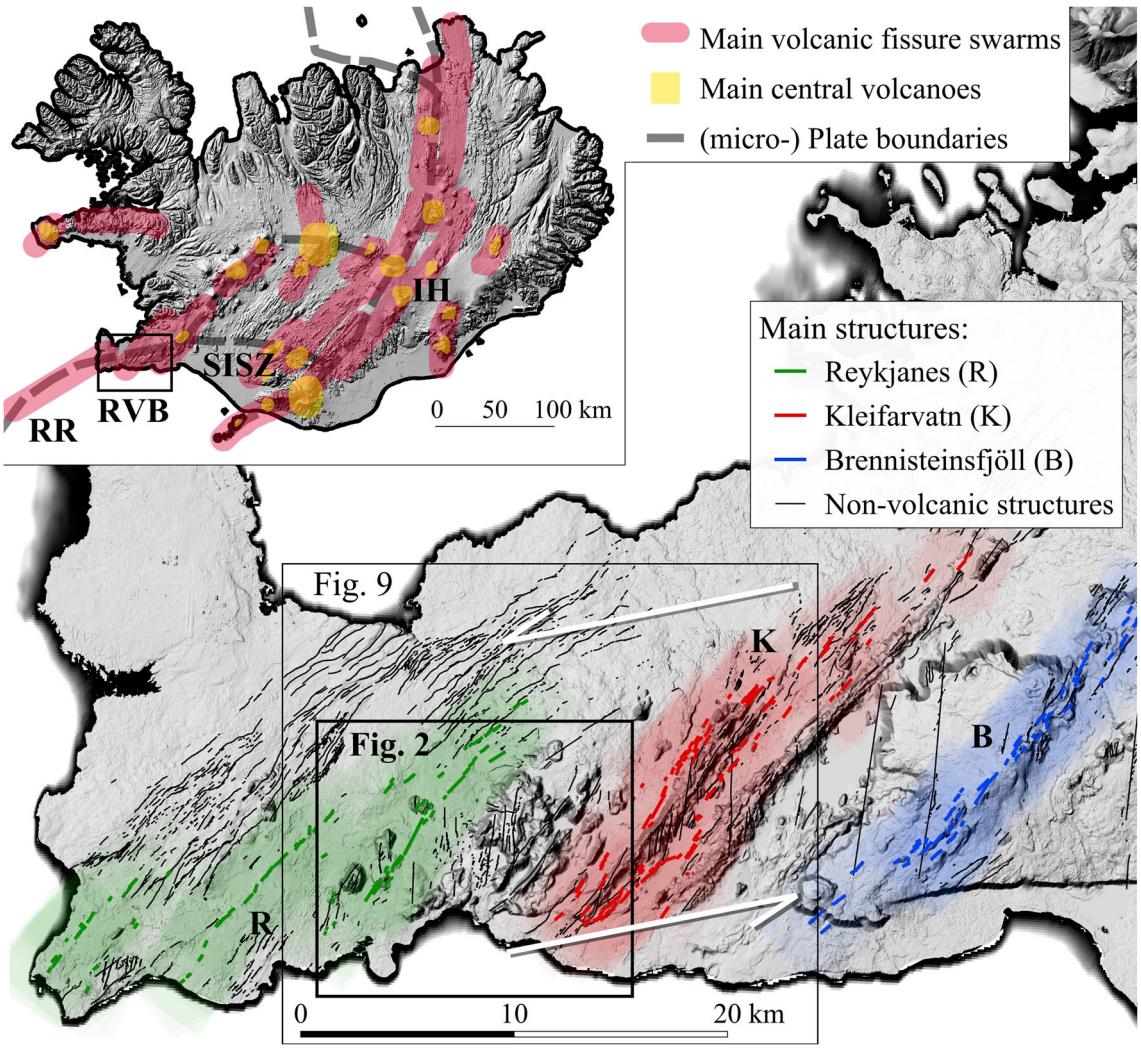

Fig. 1 Main tectonic and volcanic structures on the western Reykjanes Peninsula (from Clifton and Kattenhorn 2006). Fractures are shown in black, while the three volcanic systems are displayed in color. **Inset:** main seismic and volcanic structures in Iceland (modified from Jóhannesson and Saemundsson 1998 and Thordarson and Larsen 2007). The basemap uses the hillshade from the National Land Survey of Iceland (ÍslandsDEM, with 2 m resolution:dem.lmi.is/mapview/?application=DEM). RR: Reykjanes Ridge; RVB: Reykjanes Volcanic Belt; SISZ: South Icelandic Seismic Zone; IH: Icelandic Hotspot

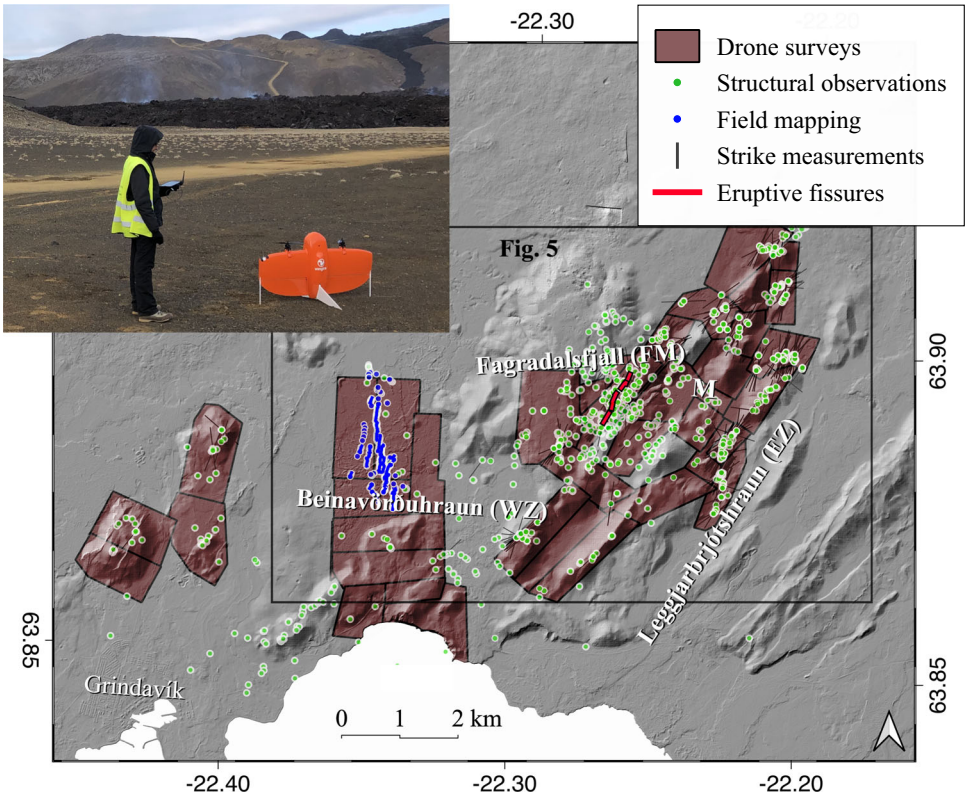

Fig. 2 Overview of the field data acquisitions. Contours represent the flight plans of our 42 drone surveys, lines show the field mapping of the West Zone rupture, and dots indicate our 1 007 field observations of ground cracks and strike measurements. Hillshade is from the ÍslandsDEM. **Inset:** E.P. operating the UAV in Meradalir (marked as 'M' on the map)

sequence (of $M_\omega = 5.6$), which occurred on February 24, 2021.

During our fieldwork, which spanned 3 weeks before the onset of the Fagradalsfjall eruption on March 19, 2021, and continued until after the peak of the volcanic activity in June 2021, we documented the gradual emergence of fractures in a 5-km radius around the eruption zone. Our objective was to gain a deeper understanding of the factors contributing to their formation, the morphological characteristics they exhibited, their spatial distribution patterns, and the chronology of their development.

Data and methods

Morpho-structural field analysis of surface deformation preceding the eruption

Starting at the end of February 2021, we carried out a morpho-structural analysis in the field and located 1 007 occurrences of ground cracks (Fig. 2), for which we measured strike, size, extensional offset, and potential strike-slip component. We corrected all the magnetically measured strike data with a declination of −12.75°, following the WWM (2019–2024 World Magnetic Model) applied for 2021-04-01 at −22.3° E; 63.85° N.

We dated ground fracturing by documenting, for example, ground cracks on previously undisturbed dirt roads or fractures crossing fresh snow patches. We then associated these data with earthquake location, timing, and magnitude information (available online at skjalftalisa.vedur.is/#/page/map) to link ground fracturing to the seismo-volcanic events that caused them. In well-consolidated substrates, we could estimate the precise direction of shear using the asperity-fit method, which consists in identifying distinct irregularities, or "asperities," along one side of a fracture, and then locating their mirror images on the other side of the fracture. By measuring the azimuth and distance between these matching asperities, we determine the direction and magnitude of the displacement or opening that has occurred along the fracture.

We installed two extensometers on a dormant fracture at the location of the second vent (Fig. 2) to track its opening over time. Each device consists of two pegs planted in stable rock on either side of a fracture situated between the first (south) and second (north) vent of the eruptive fissure. The spacing between the pegs (approximately 5 m) was measured regularly until they were covered by a lava flow (Fig. S2).

Drone imagery of deforming areas around the eruptive fissures

From March 2021 to May 2021, we conducted repeated airborne surveys of the zones where our fieldwork had revealed

the presence of ground cracks, using a Wingtra® fixed-wing UAV (Unmanned Aerial Vehicle), categorized as a *Tailsitter Vertical Take-Off and Landing* (see Fig. 2, inset). Under optimal conditions, the drone can cover 1.2 km^2 per flight, with a resolution of ∼1.5 cm/pixel and a swath-width of ∼ 100 m. We planned the flights to optimize battery life, which can last up to 50 min in windless conditions and above flat ground, but only about 25 min in cold temperatures and windy weather. We selected each area to maintain the most constant altitude or to allow a slope gradient perpendicular to the flight lines. The UAV captures images with a Sony RX1RII, 35 mm, full-frame, 42 MP camera, at an altitude of 90–120 m AGL (Above Ground Level). This elevation range is a compromise between a sufficient number of overlapping images of the highest topography, optimal pixel precision at the lowest altitude, and the largest possible area of coverage. The flight plans involve a forward and lateral image overlap of 70%.

Images are georeferenced with a 2–3 cm accuracy by GNSS (Global Navigation Satellite System) using the PPK (Post Processing Kinematic) technique via the internal software provided by Wingtra®. This technique is based on differential calculations between a temporary GNSS base of known position and a GNSS antenna onboard, recording the location data on the camera SD card. This method has the advantage of not requiring GCPs (Ground Control Points) nor communication between the base and the UAV. Agisoft Metashape® was utilized to produce georeferenced orthomosaics with a resolution of 1–2 cm/pixel, which we used for fracture mapping. We also produced digital terrain models (DTMs) with 3–4 cm accuracy.

Our orthomosaics were used in synergy with other aerial imagery datasets acquired during the tectonic unrest, including those from the Near Real-Time Photogrammetric Monitoring by Náttúrufræðistofnun Íslands (The Icelandic Institute of Natural History – hereafter IINH data), conducted in collaboration with the University of Iceland and the Land Survey of Iceland (Pedersen et al. 2022). We georeference these datasets using GCPs set up in the field or extracted from the drone images, as well as through kinematic GNSS campaigns during our field visits. We produced image correlations using the command `"$mm3d MM2DPosSism"` in the MicMac software, allowing us to characterize and quantify the deformation between acquisition times.

From our orthomosaics, we manually mapped the ground cracks of the East Zone as lines on a vector layer in QGIS (Fig. S1). Figure 3a and b show an example of a portion of an orthomosaic before and after mapping, and Fig. 3c and d illustrate the scale at which mapping was carried out (1:80 on screen). To minimize errors introduced by subjective choices and interpretation biases, one operator performed all mapping. If a fracture has only minor changes in direction, but one clear strike, we mapped it as one straight line. If a fracture is composed of two or more segments with different strikes, we mapped each segment separately. We chose not to automatize this process, as the tests we performed were excessively noisy, but the resulting dataset is available to train a neural network and make this process automatic in future projects (see Fig. S1).

We used our DTMs during the interpretation stage, mostly in the West Zone, to highlight morphologies related to fault motion, such as "push-ups," used here as a term to denote topographic uplifts forming at the surface along a fault, where geometric irregularities locally produce a compressional context (e.g., Sylvester and Smith 1976; Christie-Blick

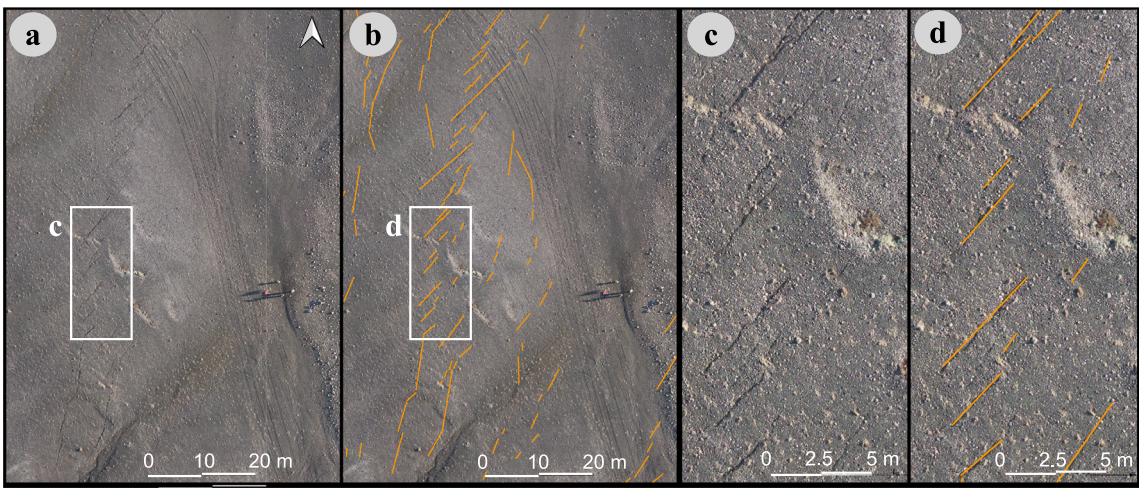

Fig. 3 Mapping using orthomosaics: example from Meradalir (see location 'M' on Fig. 2). **a)** Before mapping, with visible team members and tire marks. **b)** After mapping the tectonic features. **c)** Close-up image displaying the scale at which the orthomosaics were scrolled (1:80 on screen). **d)** The same area after mapping

and Biddle 1985; Sylvester 1988). The DTMs also helped us to keep track of the topographic context, allowing us to take into account and exclude the gravitational and ground-shaking components of the fractures, frequently observed along the slopes and at the summit of the hills.

Deformation mapping with SAR

To track the spatial and temporal evolution of the surface deformation related to the seismic activity, we processed all available 6-day Sentinel-1 Synthetic Aperture Radar (SAR) image pairs on both descending (155) and ascending (16) tracks during 21-02-17–21-03-21. To reduce noise, the interferograms were multi-looked to obtain a square pixel of $\sim 15\ m \times 15\ m$ and filtered with an adaptive filter. We downsampled the 2-m-resolution ÍslandsDEM (atlas.lmi.is/mapview/?application=DEM) to remove the topographic phase component and geocode the final maps. We mapped discontinuities produced by the earthquakes in the interferometric fringes, excluding processing artifacts by checking that (i) fringes can be seen in non-filtered interferograms, (ii) do not coincide with topographic gradients, and (iii) appear in multiple interferograms from independent images and varying viewing angles. They were also cross-checked with structures mapped or visible in the ÍslandsDEM or optical images.

Results

Our field observations enabled us to categorize anelastic deformation into two primary modes:

1. Ground cracks, which are characterized by open fractures ranging from a few millimeters to 30 cm in width and several decimeters to 10 m in length. These are distributed throughout the area, with closer spacing in regions exhibiting greater deformation. They were particularly extensive in the softer ground of the East Zone.
2. Surface ruptures, which span several hundred meters and are most noticeable in the recent lava flows of the West Zone. In the East Zone, they might be hidden beneath the approximately 5-m-thick volcano-sedimentary layer.

Widespread ground cracks in unconsolidated substratum

About 90% of the surface fractures that we observed can be classified as open cracks, indicating a component of extensional deformation. In about twenty cases, we reported significant vertical offset, forming characteristic extensional features, such as micro-grabens of about 3 m in width, 10-20 m in length, and delimited by two conjugated fractures displaying vertical offsets of up to 12 cm (Fig. 4g).

Most open fractures also exhibited a dextral shear component, with decimeter-scale doglegs within the cracks displaying subsidence (Fig. 4a), opening (Fig. 4b), or uplift (Fig. 4c), characteristic of strike-slip systems. Their spatial distribution was also characteristic of a diffuse right-lateral strike-slip system, with a generalized en-échelon arrangement (Figs. 4f, 6d). The asperity-fit technique (Fig. 4b, f) revealed right-lateral shear on both N170±10 and N035±10 fractures systems. We saw no evidence of sinistral shear.

Among the shear markers visible in the East Zone, transtensional structures were approximately ten times more numerous than transpressional ones (Fig. 4c, d). The latter were widely distributed across the study area, and typically formed larger pressure ridges at relays between two en-échelon transtensional fractures, with spacings of 1 to ~10 m. In contrast, transtensional ground fractures were typically of centimeter- to decimeter-scale (Fig. 4a, b, e, f, g).

Our drone mapping confirms the field observations, where we do not see a significant number of extensional markers, such as ground cracks, near the eruptive fissure (Fig. 4f). Instead, surface fractures were primarily concentrated a few kilometers away to the east and west of the eruptive fissure (Fig. 5).

In the East Zone, we mapped nearly 20 000 ground cracks over a 5 km^2 area (Fig. S1). They appear as open fractures ranging from a few millimeters to 30 cm in width, a few decimeters to 10 m in length, and spaced down to a few meters, although isolated incidences were recorded. Approximately 50% of these cracks are shorter than 3.6 m, and 75% are shorter than 6.5 m (Fig. 8a). Although striking in a ~N030 direction (63% of them strike between N010 and N050), they mostly align in a ~N-S trend (Figs. 4e, 6, 8c), i.e., at an angle of about 30° with respect to the overall direction of the cracks. Notably, around 5 000 of these cracks aligned along a ~3.5-km-long belt of a few tens of meters wide, located at the center of the East Zone, striking N175 and displaying over 1 000 cracks/ha (Figs. 6a, b, 8c).

Surface ruptures in hard ground

In the West Zone, we observed highly localized deformation concentrated on about eight primary fault segments of metric width, along with some secondary surface ruptures (Fig. 7d). The primary segments measure around 300–400 m in length, strike ~N015, and they repeat in an en-échelon pattern spaced 50–100 m apart, with overlaps exceeding 100 m. These segments collectively form a deformation belt approximately 200 m in width and 2 km in length, striking N175. Although their obliquity is less marked than that of the ground cracks of the East Zone, they likewise strike obliquely to the direction of the entire fault system: out of the 3 800 meters

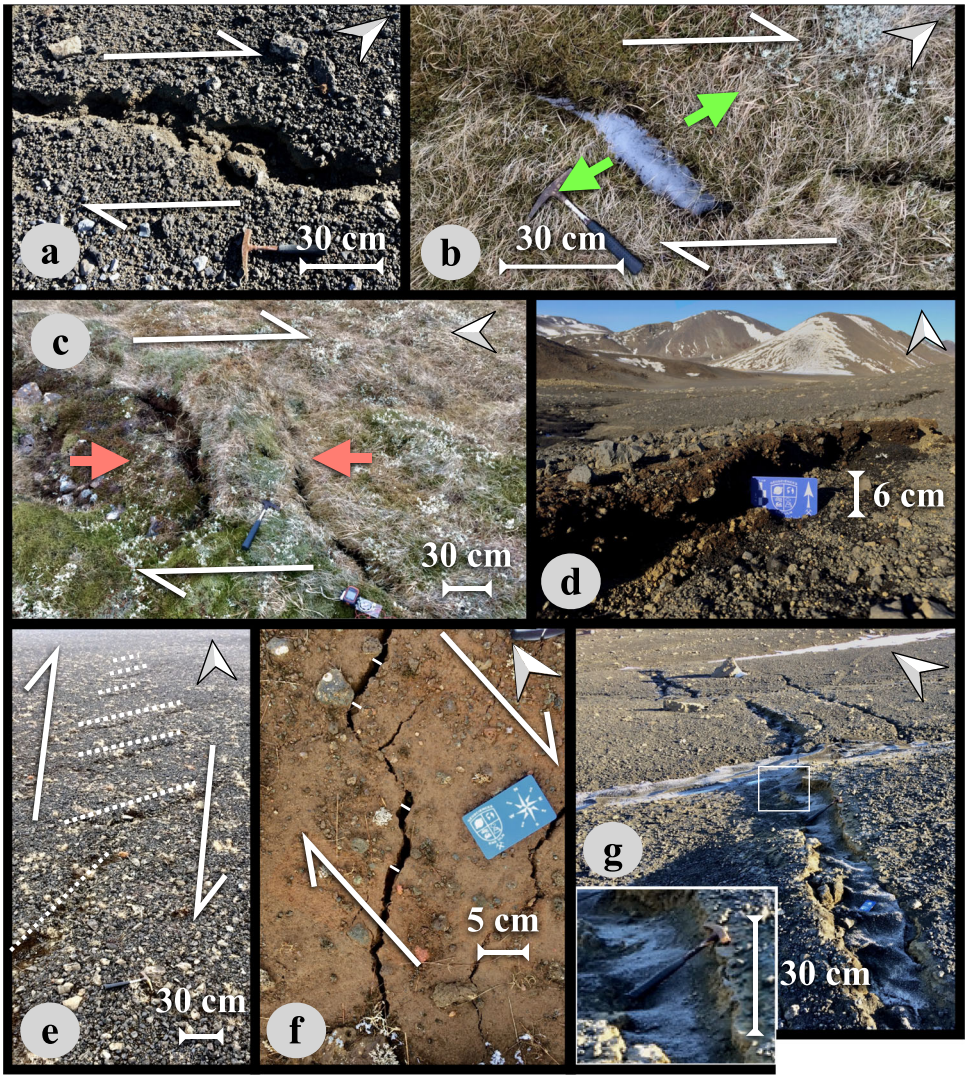

Fig. 4 Field observations of ground cracks (hammer of 31 cm for scale). See location in orange on Fig. 5. **a)** Field evidence of dextral strike-slip shear: decimeter-scale extensional relay in the soft ground of Meradalir. **b)** Same structure on an N-S fracture on the Mount Fagradalsfjall, in a rare occurrence of soil. **c)** Decimeter-scale compressional relay on the same fracture, about 10 m to the North. **d)** Same structure in the soft ground of Meradalir. **e)** En-échelon system of meter-sized ground cracks, individually striking approximately N030 but displaying an approximately N-S right-lateral sense of shear. **f)** One of the few examples of ground fracturing directly around the eruption site (at the location of the third vent, a few weeks before its emplacement). The open fractures strike approximately N030, similar to the dike direction, but the asperity-fit technique in the consolidated soil shows an approximately N170 dextral strike-slip. **g)** Field evidence of extension: eastern border fault of a micro-graben located in the East Zone, with a 12 cm vertical offset. The unconsolidated nature of the ground is visible and explains the short duration of the surface expression of these structures

of reactivated fractures that we mapped, 63% strike between N005 and N025, i.e., with a ~20° obliquity with respect to the N175-striking main fault (Fig. 8d). Along these structures, several showed clear signs of fresh reactivation, such as ploughed soil or overturned lichens (Fig. 7a). The asperity-fit technique (e.g., Fig. 7e) allowed us to estimate a recent dextral strike-slip motion of a few tens of centimeters in a direction N160-N170, confirmed by optical imagery correlation (Fig. 7b).

A series of push-ups of a few tens of centimeters to about 8 m in height and 50 m in width serves as dextral transpressive relays between these fault segments (Fig. 7c, f, g). Our DTM highlights at least four other preexisting N-S right-lateral strike-slip faults across the West Zone (Clifton and Kattenhorn 2006; Hreinsdóttir et al. 2001; Einarsson et al. 2020), that are also evident from a series of push-ups. Their cumulative offsets, measured both from the field and on the DTM, reach a few meters on various fault segments, and up to 15 m, suggesting the occurrence of several seismic ruptures since the emplacement of the lava flows, i.e., since early postglacial times (8–15 ky). This type of strike-slip fault system, with short-spaced compressive en-échelon relays, has also been reported by Einarsson et al. (2020) at the South Icelandic Seismic Zone (SISZ in Fig. 1).

We propose that the difference in morphology between these surface ruptures and the ground cracks of the East Zone is mainly due to a different nature of the ground. While the surface of the West Zone is characterized by basaltic lava flows with ages younger than 15 ky, the substratum of the East Zone is mostly unconsolidated hyaloclastite covered by several meters of unconsolidated tephra deposits and volcanic-derived sediments.

Timing of surface deformation from InSAR time series

Our analysis of the interferograms produced for the period February 17–March 21 allows us to characterize the spa-

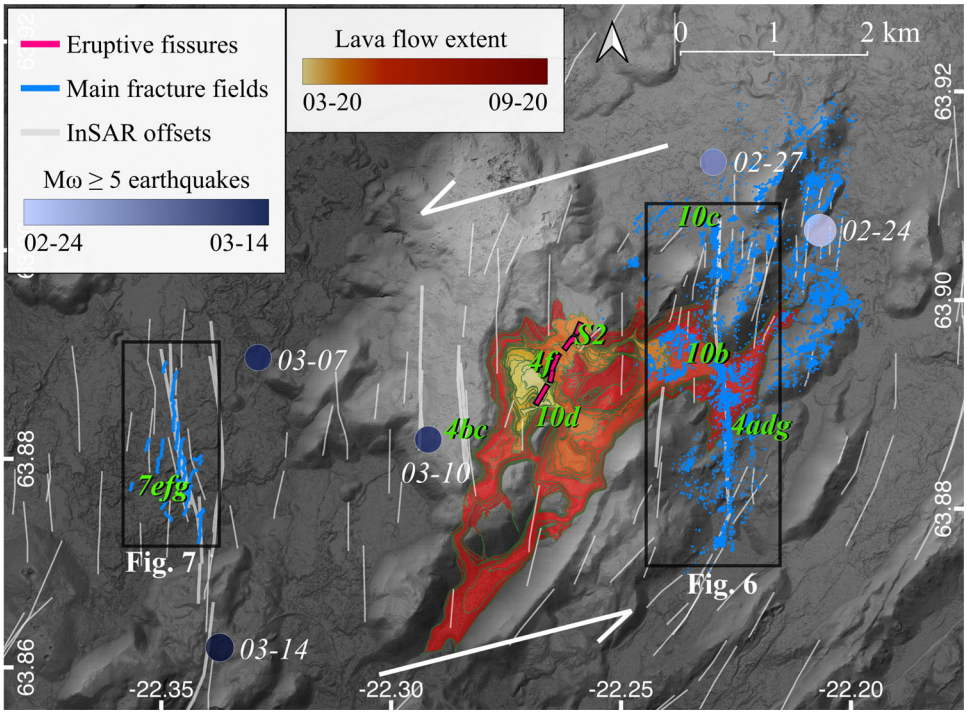

Fig. 5 Surface rupture of the West Zone (light blue; mapped in the field) and ground cracks of the East Zone (light blue; mapped from the orthomosaics). In pink the traces of the eruptive fissures; in light gray the discontinuities mapped from the InSAR data. Circles represent the locations of the $M_\omega \geq 5$ earthquakes (Sigmundsson et al. 2022), with a date-dependent color code ranging from light blue on February 24 to dark blue on March 14. Lava flow extent is from Pedersen et al. (2022) and eruptive fissures from Hjartardóttir et al. *(this special issue)*. Base layer is the ÍslandsDEM rugosity map

tiotemporal evolution of the elastic and brittle deformation generated by the dike intrusion and the main earthquakes, and to suggest a preliminary chronology for the ground fracture development. The main deformation event started on February 24 in the East Zone, associated with a $M_\omega = 5.6$ event, which was the mainshock of the 2021 seismic swarm. The ascending and descending interferograms of February 19–25 and February 23–March 1 (Fig. 9b, c) show a significant fringe discontinuity in the easternmost area (EZ1 on Fig. 9), indicating that most ground deformation took place in this area. The low InSAR coherence in EZ1 is consistent with the formation of new fractures that likely altered the backscattering power of the surface, in addition to the light snowfall that occurred at this time, but which was more widespread.

In the 20 days following the mainshock, over 60 earthquakes of $M_\omega > 4.0$ took place, with seven of them being > 5.0. Faulting associated with these earthquakes produced unambiguous discontinuities of the fringes in our interferograms (Fig. 9d–i), mainly in the region west of the Fagradalsfjall eruptive centers. In general, the largest earth-

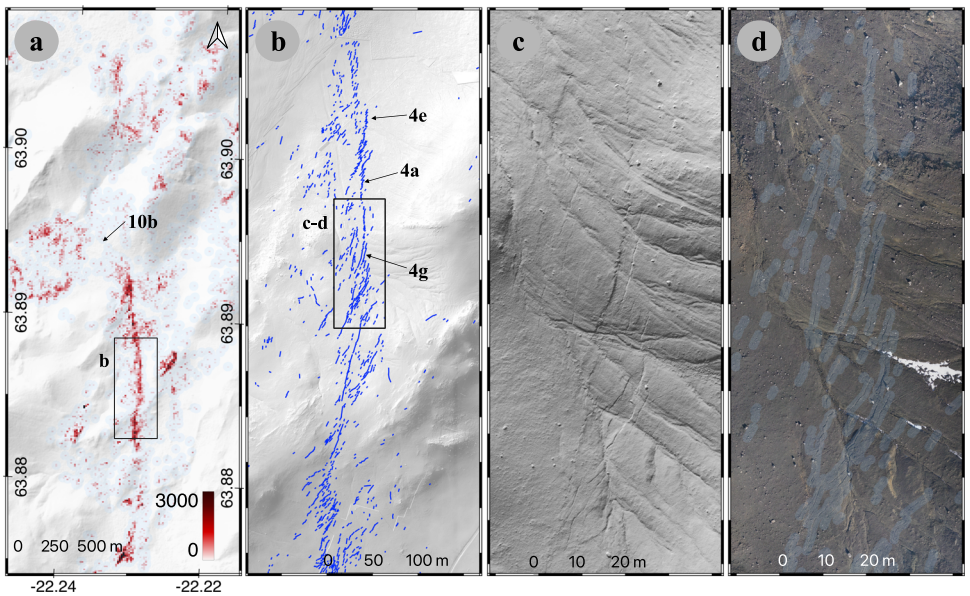

Fig. 6 Diffuse ground fracturing in the East Zone. **a)** Complete near-surface rupture of the $M_\omega = 5.6$ February 24 earthquake, with color code indicating the density of mapped cracks per hectare. **b)** Close-up of a characteristic morphology, mapped from the orthomosaics. **c)** Hillshade from the UAV DTM. **d)** Orthomosaic of the same area, with the mapped cracks highlighted in blue

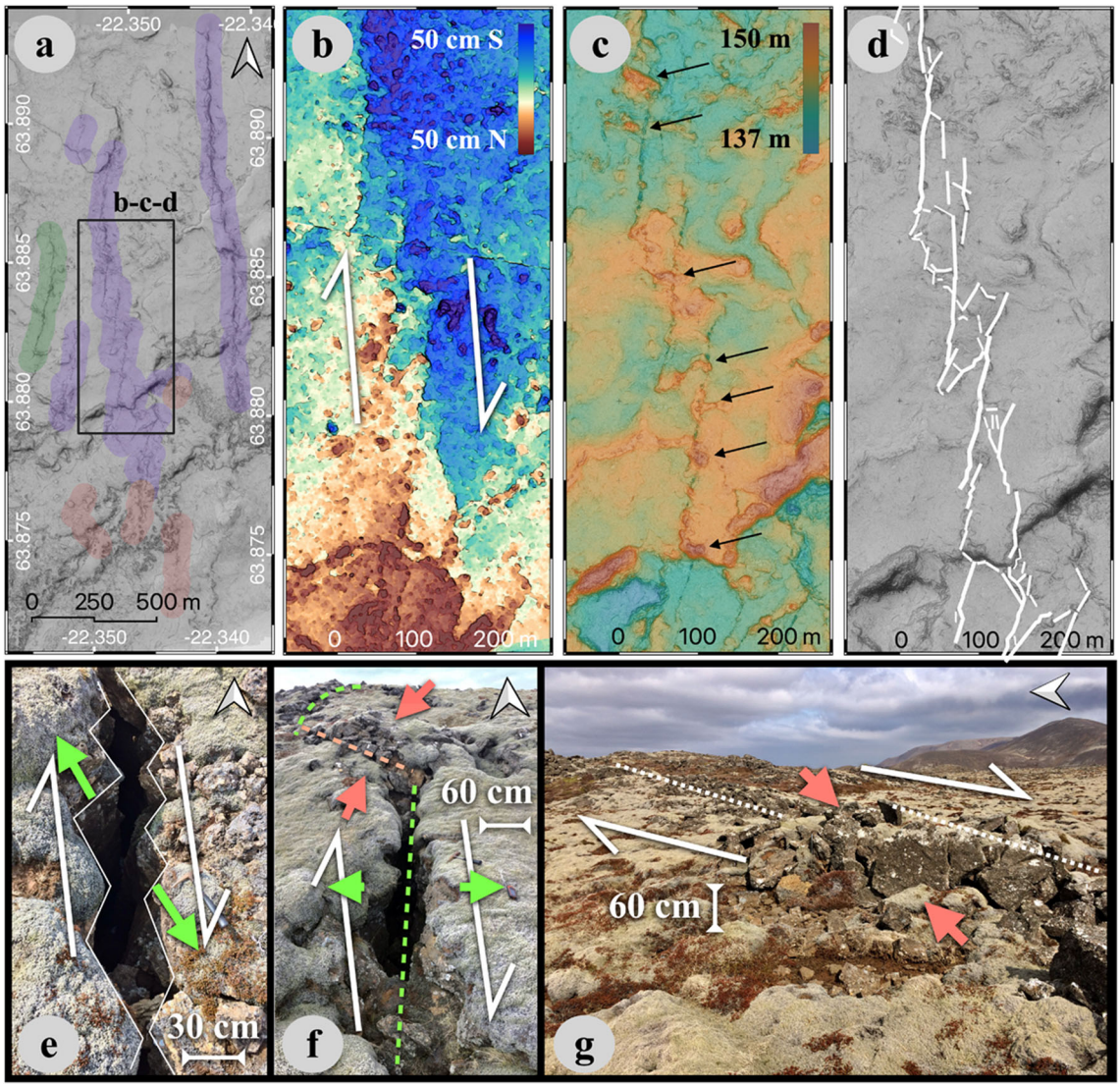

Fig. 7 Surface fractures in the West Zone. **a)** Post-tectonic hillshade processed from UAV images. Field mapping: in green pre-existing, non-reactivated fractures (see Fig. 10d), in purple pre-existing but reactivated (e.g., Fig. 7e, f); in red newly-formed. **b)** N-S displacement from pixel correlation between images from 2019 (Loftmyndir ehf., loftmyndir.is) and 7 March 2021 (Pedersen et al. 2022). **c)** Post-tectonic UAV hillshade with arrows pointing to the push-up structures. **d)** Fracture mapping from the field. **e)** Asperity-fit technique applied to a reactivated fracture (hammer of 31 cm for scale). **f)** Push-up structure on a reactivated fracture. **g)** 300-m-long fracture in the hard ground of the West Zone, striking N175. While the presence of moss inside the fracture indicates its preexistence, overturned lichens suggest a recent reactivation

quakes activated strike-slip faults distributed along the N070 plate boundary direction, with one nodal plane systematically striking roughly N-S, in accordance with the seismic results of Fischer et al. (2022).

Deformation associated with the intrusion of the dike first appears between February 23 and March 1 (Fig. 9c), and is evident in all subsequent interferograms (Fig. 9d–i), as previously imaged by Sigmundsson et al. (2022). Our data confirms that the intrusion originated from the ENE at depth and migrated toward the WSW along the ridge direction, to finally reach the surface by March 19.

Discussion

A correlation between surface ruptures and seismic events

The propagation of the dike produced localized open fractures from which magma erupted (Fig. 10f), contrasting with the typical graben structures observed during magmatic intrusions (Wright et al. 2006; Ruch et al. 2016). These fractures opened 4 km west of the East Zone, and their eruptive chronology has been extensively detailed (Hjartardóttir et al.,

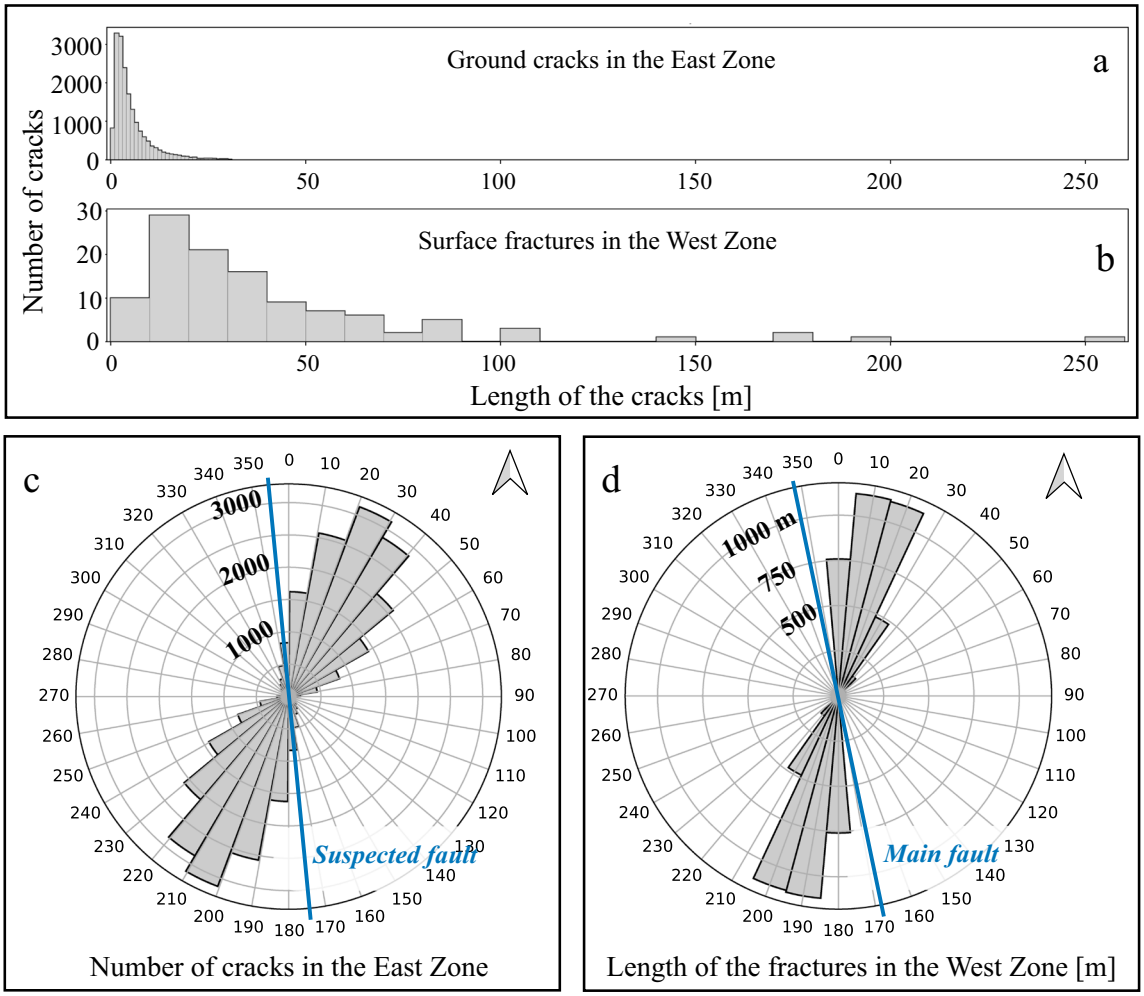

Fig. 8 Length of the mapped cracks in the East Zone **(a)** and West Zone **(b)**, in meters. **c)** Orientation of all mapped cracks in the East Zone (17,829) versus the global orientation of the suspected fault. **d)** Orientation of the mapped surface fractures (weighted by their lengths, in meters) vs the main fault strike

this special issue). The initial eruptive fissure opened on March 19 at around 20:30 UTC, roughly two days after the seismicity ceased (Pedersen et al. 2022; Fig. 10a). Seventeen days later, on April 5, another eruptive fissure opened about 1 km north of the initial eruption site. Over the next eight days, several vents opened between the initial and northern eruptive fissures (Hjartardóttir et al., *this special issue*). The fractures surrounding the volcanic vents generally did not open further during the eruption. Our two extensometers also showed that a dormant fracture located at the exact location of a new vent remained inactive even minutes before the eruption commenced (Fig. S2).

While direct volcanic-triggered fractures were rare, we find that all earthquakes with $M_\omega \geq 5.0$ and multiple clusters of $M_\omega \geq 4.0$ events resulted in surface fracturing during the tectonic unrest. We were able to link most observed surface fractures areas to specific earthquakes (e.g., Fig. 10e). Notably, we propose that the main belt of dense ground cracks in the East Zone represents the rupture location of the February 24 $M_\omega = 5.6$ earthquake, despite its epicenter being located 1.2 km to the northeast (Fig. 5; Sigmundsson et al. 2022).

In the West Zone, IINH conducted an aerial survey of the area approximately 10 h after the March 7 $M_\omega = 5.2$ earthquake. We find that most, if not all, of the recent slip on the northern portion of this fault had already occurred by noon on March 7. Most of the surface rupture in the area had previously been attributed to the March 14 $M_\omega = 5.3$ earthquake (Sigmundsson et al. 2022). However, we find that the March 14 event only caused a rupture of the southern part of the fault, while the offset affecting the northern portion of the fault corresponded to the coseismic slip during the March

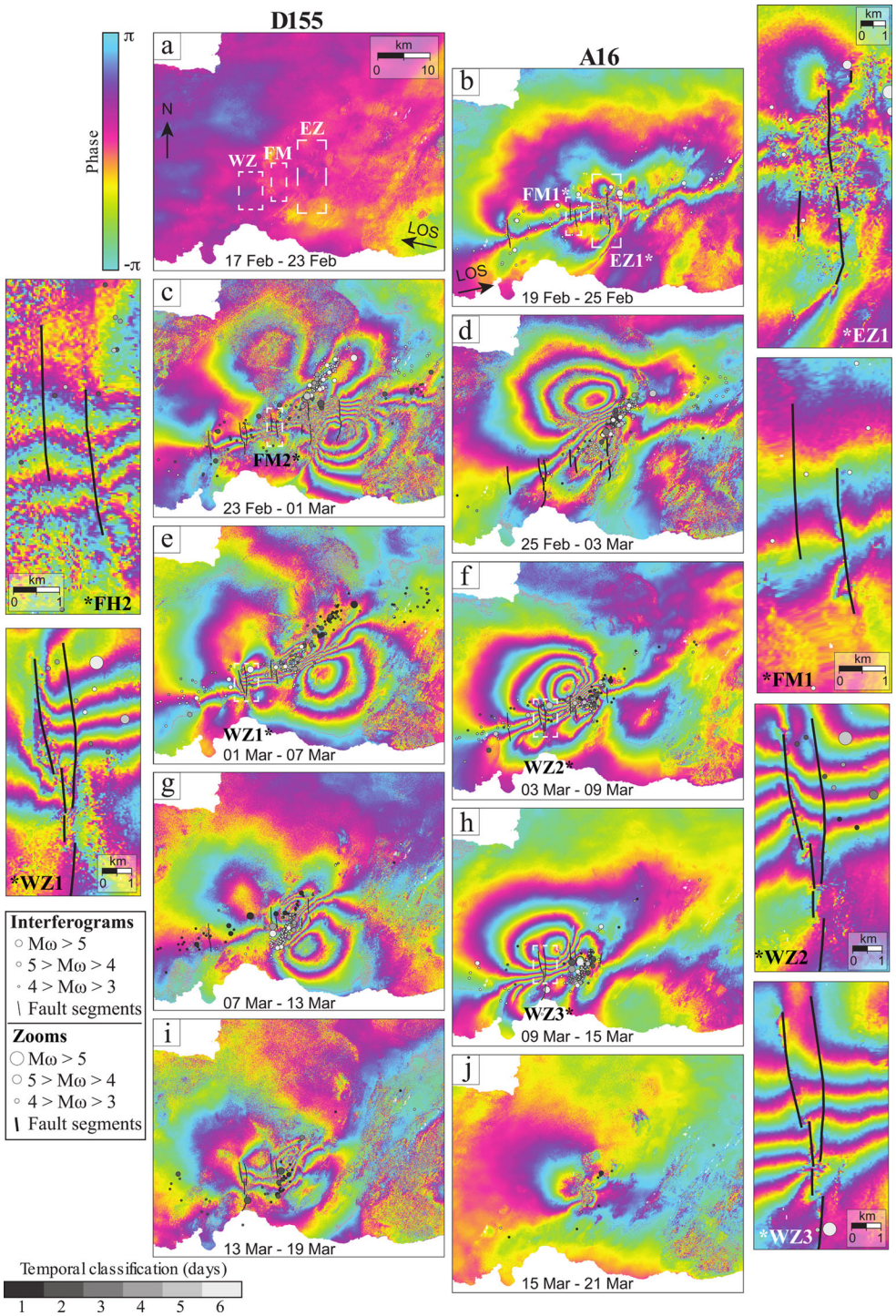

Fig. 9 Sentinel-1 filtered SAR interferograms covering the period from February 17 to March 21. The center-left column displays the descending orbit (155), while the center-right column shows the ascending orbit (16). Each interferometric pair spans 6 days. The color cycles indicate motion along the line-of-sight direction (LOS), counted positive away from the satellite. Each phase cycle corresponds to a relative displacement of approximately 2.8 cm. The left and right columns display close-ups of the East Zone (EZ), West Zone (WZ) and Mount Fagradalsfjall (FM) during various activation periods, as highlighted by white dashed rectangles on the corresponding interferograms (e.g., EZ1, EZ2...). Circles represent the epicenters of earthquakes located by the IMO, categorized by size according to magnitude ($3 \leq M_\omega \leq 5.6$) and by color according to time (from dark to light). Black lines denote the activated faults during the 6-day timespan of the interferograms

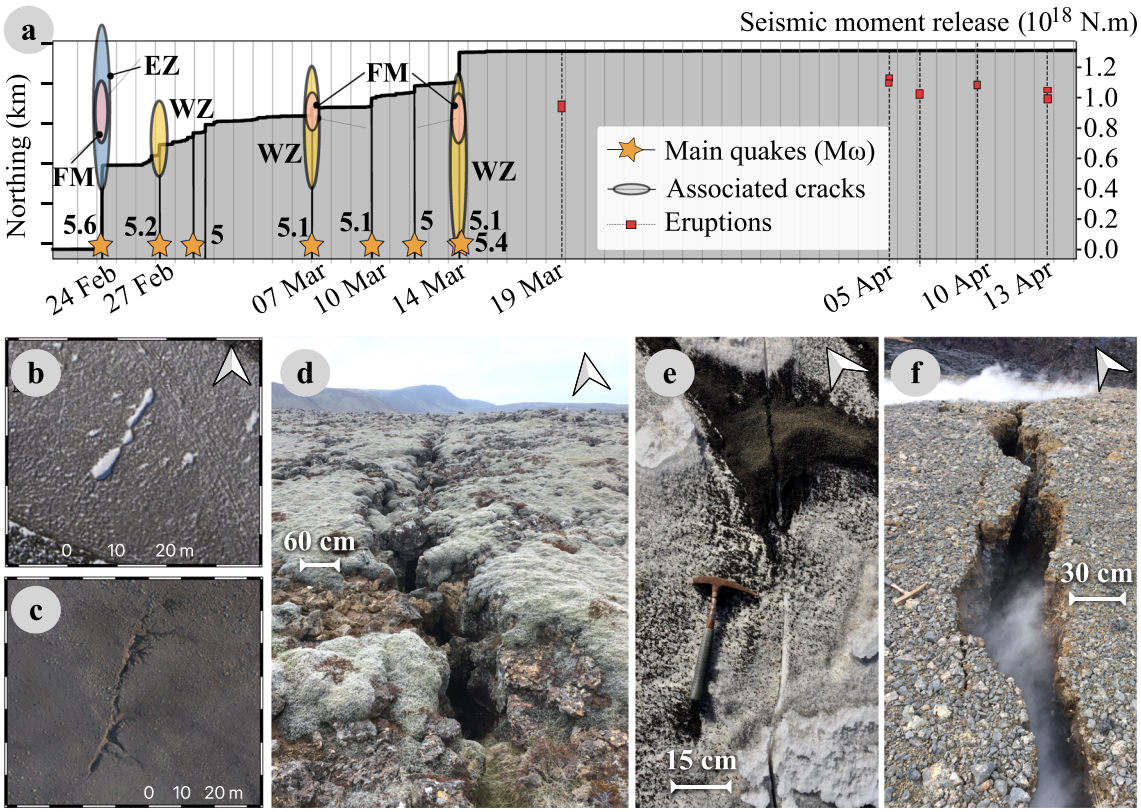

Fig. 10 Time evolution of the ground rupture and seismicity during the 2021 seismotectonic and volcanic event in Fagradalsfjall. Three main areas of fault activity are identified: the East Zone (EZ), West Zone (WZ), and Mount Fagradalsfjall (FM). Earthquakes with a magnitude $M_\omega \geq 5.0$ are represented by stars, while the corresponding ground fracturing is illustrated by elongated ellipses, with the long axis denoting the extension in the northward direction (northing; km). Throughout the tectonic unrest, all three areas experienced reactivation during up to three major events and several minor ones, with a discernible southward migration of the fracturing observed in the WZ. **b)** Orthomosaic of a pre-existing sinkhole, now covered by the lava field (see location on Fig. 6a). **c)** Orthomosaic of a newly-formed sinkhole (see location on Fig. 6a). **d)** Pre-existent, non-reactivated fracture in the West Zone (hammer of 31 cm for scale). **e)** Snow patch fractured by a recent ground crack in the East Zone. **f)** Eruptive fissure of the March 19 vent, striking N030

7 earthquake (and possibly rapid post-seismic slip occurring within hours after the mainshock), despite its epicenter being located 1 km to the northeast (Fig. 5).

Overall, our data show that surface fractures are offset by approximately 1 km to the east from the locations of earthquakes that generated them. This could be a result of the local seismometer network becoming saturated by large earthquakes, causing their P-wave arrival times to be lost in the noise created by their precursors. Alternatively, it could indicate that the observed strike-slip faults are not vertical and possess a dip of about 75° to the east, assuming a hypocenter situated 4 km below the surface.

Multiple activations of pre-existing faults

Our InSAR data reveal that most N-S-oriented fault segments experienced multiple activations (Fig. 9). In the West Zone, discontinuities are evident in almost all ascending and descending interferograms between February 23 and March 19. The fault segments were reactivated after February 23, where no signal was apparent in the first ascending interferogram (Fig. 9a), but were inactive between March 7 and 13, when no signal was found in the descending interferogram (Fig. 9g). The West Zone also displays a southward migration of fracturing during successive fault activations (Figs. 9, 10a). These trends suggest an overall southwestward migration of seismicity along the plate boundary on north-striking faults from February 24 until the onset of the eruption, in accordance with Fischer et al. (2022).

In the East Zone, the mainshock occurred below unconsolidated sediments that had not preserved any traces of earlier fault activity. A sole pre-existing sinkhole alignment in Meradalir (Fig. 10b), reactivated during the 2021 event, is now buried beneath the new lava field. This was the only evidence that a fault preexisted at this location. It is worth noting that a year after the event, most of the mapped cracks in the unconsolidated material of the East Zone were no longer preserved, except for a new sinkhole in the northern part of the zone

(Fig. 10c). This observation raises the question of how many buried faults are present in the region.

Insights into the geometry of oblique plate boundaries

With its multiple orientations of magmatic and tectonic structures, the Reykjanes Peninsula illustrates several geological and tectonic mechanisms that come into play in determining the geometry of oblique extensional plate boundaries. We observed that deformation occurs in similar patterns at three different scales, involving strike-slip tectonics with en-échelon systems: (i) at the outcrop scale with the ground crack systems in the East Zone, (ii) at the fault scale with the ruptures in the West Zone, and (iii) at the scale of the peninsula, which involves en-échelon magmatic systems with a 25° obliquity with respect to a theoretical, purely extensional rift. These systems likewise accommodate the extension component along the 70°-oblique plate boundary.

The 2021 dike intrusion at Fagradalsfjall propagated predominantly vertically, with internal migration only occurring along the fissure, i.e., oblique to the plate divergence, as revealed by the seismicity (Sigmundsson et al. 2022; Fischer et al. 2022). In contrast, dikes at divergent plate boundaries generally tend to propagate laterally from a central volcano, striking perpendicularly to the plate divergence and feeding fissure swarms that radiate from the central volcano. This has been observed, for example, in the North Iceland volcanic zone (Sigurdsson et al. 1980; Sigmundsson et al. 2015), in the Afar region (Hamling et al. 2009), and at Nyiragongo volcano (Komorowski et al. 2002; Smittarello et al. 2022). Our analysis of the 2021 Reykjanes Peninsula event thus offers the opportunity to investigate the direct influence of a volcanic intrusion on a seismo-tectonic system, by disengaging from the influence of a central volcano, which partially determines the morphology of the fractures (Trippanera et al. 2017; Sigmundsson et al. 2015; Paquet et al. 2007).

Our data also tackles the relationship between rift obliquity and strike-slip faulting. Understanding the factors determining whether a given system deforms through bookshelf faulting, oblique shear, or pull-apart, usually necessitates a deeper understanding of the rheological properties of the system (Feighner and Richards 1995; Zwaan and Schreurs 2017; Phillips et al. 2019; Fossen et al. 2017). In continental rifts (e.g., the Afar region), inherited crustal anisotropies tend to channel the rift location (Corti 2008; Maestrelli et al. 2020), which is not the case in oceanic rifts such as Iceland, where the crust is more homogeneous, as it is essentially magmatic (Jones 2003; Darbyshire et al. 2000; Hardarson et al. 1997). Instead, the geometry and morphology of oceanic ridges are largely dictated by dike intrusions that generate graben structures and eruptive fissures. Comparing the structures that we observed in the context of magmatic and 70°-oblique, sinistral shear, with the ones formed at less oblique rifts in North Iceland, especially during the 2014 Holuhraun eruption, with a 19° obliquity (Ruch et al. 2016), may enable us to distinguish the direct effects of the dike injection from those of the strike-slip plate boundary on the formation of systems of strike-slip faults and surface fractures around a rift eruption.

Finally, we emphasize that the structures we observed at the Reykjanes Peninsula exhibit good continuity with the amagmatic South Icelandic Seismic Zone (SISZ in Fig. 1). This fault zone, which extends from the east of the Reykjanes Peninsula (RVB) toward the Icelandic Hotspot (IH), is characterized by dozens of parallel dextral strike-slip faults striking in a N-S direction (Einarsson 2010; Einarsson et al. 2015; Hjartardóttir and Einarsson 2015). These faults intersect the plate boundary almost orthogonally and have been activated repeatedly in historical times (Einarsson et al. 2020). They accommodate the sinistral shear of the plate boundary in a bookshelf mode mainly revealed by alignments of metric to decametric compressive relays, similar to the one we described for the Reykjanes Peninsula. Despite being amagmatic, the eastern part of the SISZ has experienced frequent earthquakes with magnitudes of up to 7, such as the 1912 Selsund event (Bellou et al. 2005). In 2008, an earthquake doublet ($M_\omega = 6.1$) affected the western end of the SISZ, causing ground displacement and surface faulting (Decriem et al. 2010). This recurrent seismicity poses a significant risk to the local population, the Reykjavík city (300 000 inhabitants, situated a few tens of kilometers away), as well as the geothermal power plants in the area. Long-term monitoring of deformation along the faults in this zone, through the correlation of UAV-derived orthomosaics and InSAR time series, in combination with analog and digital deformation models plus a denser GNSS array, could help better constrain their kinematics and related hazards.

Conclusions

Our immediate on-site investigation of the structures related to the 2021 Reykjanes intrusive and eruptive event allowed us to capture real-time surface changes caused by an intrusion at an oblique rift system. We find that the hydraulic fracturing caused by the intrusion did not directly cause significant anelastic surface deformation, except along the eruptive fissures. Ground cracks, however, were mainly caused by the preceding earthquake sequence, highlighting the strong interaction between the magmatic system and surrounding faults at a creeping transtensional plate boundary.

Our findings also demonstrate that diffuse fracturing is a critical part of shallow deformation during strike-slip faulting. Past ruptures may show a significant *slip deficit* in the last few meters close to the surface, where the rupture is accommodated by widespread damaging of the ground. This lack

of defined surface rupture leads to a critical underestimation of the hazards associated to the faults if studying them only at the sub-surface.

Fractures observed in unconsolidated sediments produced a dense network of en-échelon cracks with metric lengths, separated by relays of metric to decametric size and exhibiting 1 to 10 cm offsets. On hard ground, surface ruptures showed a similar morphology but at a larger scale, with a series of 350-m-long "échelons," where deformation was much more localized, separated by compressional, *push-up* relays.

Our survey of the thousands of meter-sized ground cracks that formed during the 3 weeks before the Fagradalsfjall eruption reveals that, although their strikes were approximately N030, they aligned along N-S belts of approximately 3 km in length. Their spatio-temporal correlation with major ($M_\omega \geq 5.0$) earthquakes, the N-S orientation of the en-échelon structures and the widespread dextral shear morphologies at the outcrop scale indicate that these ground cracks formed through co-seismic dextral strike-slip along N-S faults, conjugated in bookshelf mode to the main shear zone of the plate boundary. Identifying these faults allows their further analysis through sub-surface geophysical techniques, such as ground-penetrating radar.

Finally, we observed that cracks formed in unconsolidated tephra deposits and volcanic sediments undergo partial erosion within a few weeks and complete erasure after less than a year. Our early investigation allowed us to map a dense network of N-S dextral strike-slip faults, that preexisted with a cumulative offset of several meters. Their meter-scale expression and poor representation in surface outcrops thus raise questions about their under-representation during hazard assessment, emphasizing the need to analyze such structures as soon as possible during such an event.

Supplementary Information The online version contains supplementary material available at https://doi.org/10.1007/s00445-023-01666-9.

Acknowledgements The authors would like to thank the Icelandic Civil Protection for the fruitful discussions that were held during the crisis, the University of Iceland (especially Páll Einarsson) for their availability on and off the field, Loftmyndir ehf. (loftmyndir.is) for the communication of their aerial images, and Andrew Harris, Emanuela De Beni and an anonymous reviewer for their precious comments.

Funding Open access funding provided by University of Geneva. JR received funding from the Swiss National Science Foundation (grant no. PP00P2_176869- TEMPO) and EP and SM are funded by the same grant in the frame of their Ph.D. projects. SB received funds from the Université Paris Cité in the framework of the MIRES mobility funds.

Data availability The vectorial files of the ground cracks mapping are fully available at the following link: https://osf.io/j2peu/?view_only=8bfdaaa6234a40b99f602db16efbb5b5. The orthomosaics and the DTMs will be added at the same link as soon as they are fully processed.

Code Availability Not applicable.

Declarations

Conflict of interest The authors declare no competing interests.

References

Bellou M, Bergerat F, Angelier J, Homberg C (2005) Geometry and segmentation mechanisms of the surface traces associated with the 1912 selsund earthquake. Southern Iceland. Tectonophysics 404(3–4):133–149

Björnsson S, Einarsson P, Tulinius H, Hjartardóttir ÁR (2020) Seismicity of the Reykjanes Peninsula 1971–1976. J Volcanol Geotherm Res 391:106369

Bourgeois O, Dauteuil O, Hallot E (2005) Rifting above a mantle plume: structure and development of the Iceland plateau. Geodin Acta 18(1):59–80

Christie-Blick N, Biddle KT (1985) Deformation and basin formation along strike–slip faults

Clifton AE, Kattenhorn SA (2006) Structural architecture of a highly oblique divergent plate boundary segment. Tectonophysics 419(1–4):27–40

Corti G (2008) Control of rift obliquity on the evolution and segmentation of the main Ethiopian rift. Nat Geosci 1(4):258–262

Darbyshire FA, White RS, Priestley KF (2000) Structure of the crust and uppermost mantle of Iceland from a combined seismic and gravity study. Earth Planet Sci Lett 181(3):409–428

Decriem J, Árnadóttir T, Hooper A, Geirsson H, Sigmundsson F, Keiding M, Ófeigsson B, Hreinsdóttir S, Einarsson P, LaFemina P et al (2010) The 2008 may 29 earthquake doublet in SW Iceland. Geophys J Int 181(2):1128–1146

DeMets C, Gordon RG, Argus DF (2010) Geologically current plate motions. Geophys J Int 181(1):1–80

Einarsson P (1991) Volcanoes in Iceland. Geologiska Föreningens i Stockholm Förhandlingar 113(1):7–19

Einarsson P (2008) Plate boundaries, rifts and transforms in Iceland. Jökull 58:35–58

Einarsson P (2010) Mapping of holocene surface ruptures in the south Iceland seismic zone. Jökull 60:121–138

Einarsson P, Sæmundsson K (1987) Earthquake epicenters 1982–1985 and volcanic systems in Iceland (map). In: Sigfússon Th (ed) Í Hlutarsins Eðli: Festschrift for Thorbjorn Sigurgeirsson, Menningarsjóður. Reykjavík

Einarsson P, Hjartardóttir ÁR, Hreinsdóttir S, Imsland P (2020) The structure of seismogenic strike-slip faults in the eastern part of the Reykjanes Peninsula Oblique Rift. SW Iceland. J Volcanol Geotherm Res 391:106372

Einarsson P, Beer M, Kougioumtzoglou I, Patelli E, Au I (2015) Mechanisms of earthquakes in Iceland. In: Beer M, Patelli E, Kougioumtzoglou IA, Au SK (eds) Encyclopedia of Earthquake Engineering,Springer, Berlin, Heidelberg

Feighner MA, Richards MA (1995) The fluid dynamics of plume-ridge and plume-plate interactions: an experimental investigation. Earth Planet Sci Lett 129(1):171–182

Fischer T, Hrubcová P, Salama A, Doubravová J, Ágústsdóttir T, Gudnason E, Horálek J, Hersir G (2022) Swarm seismicity illuminates stress transfer prior to the 2021 Fagradalsfjall eruption in Iceland. Earth Planet Sci Lett 594

Fossen H, Khani HF, Faleide JI, Ksienzyk AK, Dunlap WJ (2017) Post-caledonian extension in the west Norway-northern north sea region: the role of structural inheritance. Geological Society, London, Special Publications 439(1):465–486

Furman T, Bryce J, Rooney T, Hanan B, Yirgu G, Ayalew D (2006) Heads and tails: 30 million years of the afar plume. Geological Society, London, Special Publications 259(1):95–119

Green RG, White RS, Greenfield T (2014) Motion in the north Iceland volcanic rift zone accommodated by bookshelf faulting. Nat Geosci 7(1):29–33

Hamling IJ, Ayele A, Bennati L, Calais E, Ebinger CJ, Keir D, Lewi E, Wright TJ, Yirgu G (2009) Geodetic observations of the ongoing Dabbahu rifting episode: new dyke intrusions in 2006 and 2007. Geophys J Int 178(2):989–1003

Hardarson B, Fitton J, Ellam R, Pringle M (1997) Rift relocation - a geochemical and geochronological investigation of a palaeo-rift in Northwest Iceland. Earth Planet Sci Lett 153(3):181–196

Heezen BC, Tharp M, Ewing M (1959) The floors of the oceans, volume 65. Geological Society of America New York

Hjartardóttir ÁR, Einarsson P (2015) The interaction of fissure swarms and monogenetic lava shields in the rift zones of Iceland. J Volcanol Geotherm Res 299:91–102

Hjartardóttir ÁR, Dürig T, Parks M, Drouin V, Eyjólfsson V, Reynolds H, Einarsson P, Jensen E, Óskarsson B, Belart J, Ruch J, Gies N, Pedersen G (2023) Pre-existing fractures and eruptive vent openings during the 2021 Fagradalsfjall eruption. Bulletin of Volcanology, this issue, Iceland

Hreinsdóttir S, Einarsson P, Sigmundsson F (2001) Crustal deformation at the oblique spreading Reykjanes Peninsula, SW Iceland: Gps measurements from 1993 to 1998. J Geophys Res Solid Earth 106(B7):13803–13816

Jakobsdóttir SS (2008) Earthquake swarms at Upptyppingar, north-east Iceland: a sign of magma intrusion? Geophys J Int 172(3):976–984

Jakobsson SP, Jonsson J, Shido F (1978) Petrology of the Western Reykjanes Peninsula. Iceland. J Petrol 19(4):669–705

Jóhannesson H, Saemundsson K (1998) Geological map of Iceland. scale 1:500,000. Tectonics, Iceland Institute of Natural History, Reykjavik

Jones SM (2003) Test of a ridge-plume interaction model using oceanic crustal structure around Iceland. Earth Planet Sci Lett 208(3):205–218

Keiding M, Lund B, ÁRnadóttir T, (2009) Earthquakes, stress, and strain along an obliquely divergent plate boundary: Reykjanes Peninsula, southwest Iceland. J Geophys Res Solid Earth 114(B9):B09306

Komorowski JC et al. (2002) The January 2002 flank eruption of Nyiragongo Volcano (Democratic Republic of Congo): chronology, evidence for a tectonic rift trigger, and impact of lava flows on the city of Goma. Acta Vulcanol 1000–1035

La Rosa A, Pagli C, Keir D, Sani F, Corti G, Wang H, Possee D (2019) Observing Oblique Slip During Rift Linkage in Northern Afar. Geophys Res Lett 46(19):10,782–10,790

Le Pichon X (1968) Sea-floor spreading and continental drift. J Geophys Res 73(12):3661–3697

MacDonald KC, Fox PJ, Perram LJ, Eisen MF, Haymon RM, Miller SP, Carbotte SM, Cormier MH, Shor AN (1988) A new view of the mid-ocean ridge from the behaviour of ridge-axis discontinuities. Nature 335(6187):217–225

Maestrelli D, Montanari D, Corti G, Del Ventisette C, Moratti G, Bonini M (2020) Exploring the interactions between rift propagation and inherited crustal fabrics through experimental modeling. Tectonics 39(12):e2020TC006211. e2020TC006211 2020TC006211

Pagli C, Yun S-H, Ebinger C, Keir D, Wang H (2019) Strike-slip tectonics during rift linkage. Geology 47(1):31–34

Paquet F, Dauteuil O, Hallot E, Moreau F (2007) Tectonics and magma dynamics coupling in a dyke swarm of Iceland. J Struct Geol 29(9):1477–1493

Pedersen GB, Belart JM, Óskarsson BV, Gudmundsson MT, Gies N, Högnadóttir T, Hjartardóttir ÁR, Pinel V, Berthier E, Dürig T et al (2022) Volume, effusion rate, and lava transport during the 2021 Fagradalsfjall eruption: results from near real-time photogrammetric monitoring. Geophys Res Lett 49(13):e2021GL097125

Philippon M, Corti G (2016) Obliquity along plate boundaries. Tectonophysics 693:171–182

Phillips TB, Fazlikhani H, Gawthorpe RL, Fossen H, Jackson CA-L, Bell RE, Faleide JI, Rotevatn A (2019) The influence of structural inheritance and multiphase extension on rift development, the northern north sea. Tectonics 38(12):4099–4126

Poore H, White N, Maclennan J (2011) Ocean circulation and mantle melting controlled by radial flow of hot pulses in the Iceland plume. Nat Geosci 4(8):558–561

Ruch J, Wang T, Xu W, Hensch M, Jónsson S (2016) Oblique rift opening revealed by reoccurring magma injection in central Iceland. Nat Commun 7(1):12352

Sæmundsson K, Sigurgeirsson MÁ, Friðleifsson GÓ, (2020) Geology and structure of the reykjanes volcanic system, iceland. J Volcanol Geotherm Res 391

Sigmundsson F, Hooper A, Hreinsdóttir S, Vogfjörd KS, Ófeigsson BG, Heimisson ER, Dumont S, Parks M, Spaans K, Gudmundsson GB et al (2015) Segmented lateral dyke growth in a rifting event at bárðarbunga volcanic system. Iceland. Nature 517(7533):191–195

Sigmundsson F, Einarsson P, Hjartardóttir ÁR, Drouin V, Jónsdóttir K, Árnadóttir T, Geirsson H, Hreinsdóttir S, Li S, Ófeigsson BG (2020) Geodynamics of Iceland and the signatures of plate spreading. J Volcanol Geotherm Res 391:106436

Sigmundsson F, Parks M, Hooper A, Geirsson H, Vogfjörd KS, Drouin V, Ófeigsson BG, Hreinsdóttir S, Hjaltadóttir S, Jónsdóttir K et al (2022) Deformation and seismicity decline before the 2021 Fagradalsfjall eruption. Nature 609(7927):523–528

Sigurdsson O et al (1980) Surface deformation of the Krafla fissure swarm in two rifting events. J Geophys 47(1):154–159

Smittarello D, Smets B, Barrière J, Michellier C, Oth A, Shreve T, Grandin R, Theys N, Brenot H, Cayol V, Allard P, Caudron C, Chevrel O, Darchambeau F, de Buyl P, Delhaye L, Derauw D, Ganci G, Geirsson H, Kamate Kaleghetso E, Kambale Makundi J, Kambale Nguomoja I, Kasereka Mahinda C, Kervyn M, Kimanuka Ruriho C, Le Mével H, Molendijk S, Namur O, Poppe S, Schmid M, Subira J, Wauthier C, Yalire M, d'Oreye N, Kervyn F, Syavulisembo Muhindo A (2022) Precursor-free eruption triggered by edifice rupture at Nyiragongo volcano. Nature 609(7925):83–88

Sylvester AG (1988) Strike-slip faults. Geol Soc Am Bull 100(11):1666–1703

Sylvester AG, Smith RR (1976) Tectonic transpression and basement-controlled deformation in san Andreas fault zone. Salton trough. California. AAPG Bulletin 60(12):2081–2102

Tharp M, Heezen BC, Le Pichon X (1968) Sea-floor spreading and continental drift. Science 159(3818):309–314

Thordarson T, Larsen G (2007) Volcanism in Iceland in historical time: volcano types, eruption styles and eruptive history. J Geodyn 43(1):118–152

Trippanera D, Ruch J, Acocella V, Thordarson T, Urbani S (2017) Interaction between central volcanoes and regional tectonics along divergent plate boundaries: Askja. Iceland. Bull Volcanol 80(1):1

Tron V, Brun J-P (1991) Experiments on oblique rifting in brittle-ductile systems. Tectonophysics 188(1):71–84

Wilson JT (1965) A new class of faults and their bearing on continental drift. Nature 207(4995):343–347

Withjack MO, Jamison WR (1986) Deformation produced by oblique rifting. Tectonophysics 126(2):99–124

Wolfe CJ, Bjarnason ITh, VanDecar JC, Solomon SC (1997) Seismic structure of the Iceland mantle plume. Nature 385(6613): 245–247

Wright TJ, Ebinger C, Biggs J, Ayele A, Yirgu G, Keir D, Stork A (2006) Magma-maintained rift segmentation at continental rupture in the 2005 afar dyking episode. Nature 442(7100):291–294

Wright TJ, Sigmundsson F, Pagli C, Belachew M, Hamling IJ, Brandsdóttir B, Keir D, Pedersen R, Ayele A, Ebinger C, Einarsson P, Lewi E, Calais E (2012) Geophysical constraints on the dynamics of spreading centres from rifting episodes on land. Nat Geosci 5(4):242–250

Zwaan F, Schreurs G (2020) Viscous heating in orogenic systems: a review of rock deformation experiments. Tectonophysics 778

Zwaan F, Schreurs G (2017) How oblique extension and structural inheritance influence rift segment interaction: insights from 4d analog models. Interpretation 5(1):SD119–SD138